



# Sensitivity of Post-TAVR Hemodynamics to the Distal Aortic Arch Anatomy: A High-Fidelity CFD Study

Thangam Natarajan<sup>1</sup> · Shelly Singh-Gryzbon<sup>1,2</sup> · Huang Chen<sup>1</sup> · Vahid Sadri<sup>1,3</sup> · Philipp Ruile<sup>4</sup> · Franz-Josef Neumann<sup>4</sup> · Ajit P. Yoganathan<sup>1</sup> · Lakshmi P. Dasi<sup>1</sup>

Received: 13 September 2023 / Accepted: 22 March 2024 / Published online: 23 April 2024  
© The Author(s) under exclusive licence to Biomedical Engineering Society 2024

## Abstract

**Purpose** Patient-specific simulations of transcatheter aortic valve (TAV) using computational fluid dynamics (CFD) often rely on assumptions regarding proximal and distal anatomy due to the limited availability of high-resolution imaging away from the TAV site and the primary research focus being near the TAV. However, the influence of these anatomical assumptions on computational efficiency and resulting flow characteristics remains uncertain. This study aimed to investigate the impact of different distal aortic arch anatomies—some of them commonly used in literature—on flow and hemodynamics in the vicinity of the TAV using large eddy simulations (LES).

**Methods** Three aortic root anatomical configurations with four representative distal aortic arch types were considered in this study. The arch types included a 90-degree bend, an idealized distal aortic arch anatomy, a clipped version of the idealized distal aortic arch, and an anatomy extruded along the normal of segmented anatomical boundary. Hemodynamic parameters both instantaneous and time-averaged such as Wall Shear Stress (WSS), and Oscillatory Shear Index (OSI) were derived and compared from high-fidelity CFD data.

**Results** While there were minor differences in flow and hemodynamics across the configurations examined, they were generally not significant within our region of interest i.e., the aortic root. The choice of extension type had a modest impact on TAV hemodynamics, especially in the vicinity of the TAV with variations observed in local flow patterns and parameters near the TAV. However, these differences were not substantial enough to cause significant deviations in the overall flow and hemodynamic characteristics.

**Conclusions** The results suggest that under the given configuration and boundary conditions, the type of outflow extension had a modest impact on hemodynamics proximal to the TAV. The findings contribute to a better understanding of flow dynamics in TAV configurations, providing insights for future studies in TAV-related experiments as well as numerical simulations. Additionally, they help mitigate the uncertainties associated with patient-specific geometries, offering increased flexibility in computational modeling.

**Keywords** Transcatheter aortic valve replacement · CFD · LES · Outflow

## Introduction

Transcatheter Aortic Valve Replacement (TAVR) has emerged as a transformative procedure in interventional cardiology, offering a less invasive alternative to surgical aortic valve replacement (SAVR) for patients with symptomatic severe aortic stenosis and calcific aortic valve disease

since the first reported human implantation nearly 20 years ago [1]. In numerous large-scale randomized clinical trials, notably the PARTNER (Placement of AoRTic TraNscathetER Valve) series of trials [2, 3], TAVR has consistently demonstrated comparable or better outcomes in the short-term than SAVRs across a wide range of surgical risk profiles [4]. As TAVR continues to expand to younger, low-risk patients with longer life expectancies, several concerns including long-term outcomes of the transcatheter aortic valve (TAV), its durability, conduction-related disturbances, and associated complications such as paravalvular leak and

---

Associate Editor Jane Grande-Allen, PhD oversaw the review of this article.

---

Extended author information available on the last page of the article

subclinical leaflet thrombosis [5] are being actively investigated both experimentally and numerically.

Medical “*Image-based*” computational fluid dynamics (CFD) applied to model TAV and resulting secondary comorbidities have been largely targeted toward patient-specific treatment planning, analyzing associated hemodynamics, and optimizing procedural outcomes [6]. However, the growing use of CFD in TAVR research also presents the need to systematically study and navigate the challenges inherent to “*patient-specific*” modeling, such as incomplete patient-specific data, flow and modeling assumptions, and the uncertainty associated with raw data measurements, to arrive at meaningful conclusions or build a reliable modeling framework. In the context of modeling TAVs, they are not exempt from the aforementioned impediments and there are notable challenges that require and demand careful consideration in order to resolve the flow accurately in such complex geometries. The challenges primarily stem from two factors. First, the inherent motion within the system, encompassing the dynamic motion of the ventricles, the leaflets of the valve, and the global motion induced by pulsatile flow, adds a layer of complexity, requiring complex numerical simulations that take these into consideration. Second, owing to the TAVs location and anatomy, like most cardiovascular flow problems, obtaining the data about the shape and flow in the arterial branches off the aortic root, the coronaries, the supra-aortic vessels, the length and tortuosity of the descending aorta are not straight-forward and in most cases is unavailable or often not well segmentable. Even if obtained or assumed in most cases, the extent beyond which the anatomical features need to be truncated and its influence on the inherent flow of interest is still a challenging study.

Significant evidence demonstrates that geometric modifications downstream of a specific region can exert substantial influence on the upstream flow field. However, the extent to which this phenomenon applies to TAVR simulations, as well as the specific influence of the distal aortic arch anatomy, requires further investigation. Particularly, in many published studies, the computational domains often overlook or oversimplify the inclusion of distal aortic arch anatomies. We hypothesize that this simplification arises from the fact that the imaging data used for segmentation and surface model generation in CFD simulations primarily focuses on the region of interest directly related to TAV placement. During imaging for TAV, the resolution window is typically set to capture intricate features such as the prosthetic leaflets and stents (post-implantation) with sufficient detail. As a result, high-resolution image volumes of the TAV and its immediate vicinity are obtained, processed, and segmented with minimal error. However, the remaining thoracic region, which includes the distal parts of the aorta, is often captured at a lower resolution or may be unavailable altogether. Even when available, these regions need

to be spatially “registered” back with the high-resolution aortic root anatomy. As a result of this discontinuity in the workflow, the impact of the distal aortic arch anatomy on the overall hemodynamics in the proximity of the TAV site remains largely unexplored.

Different approaches have been employed in simulating TAVs and have utilized various types of distal aortic arch anatomies as flow extensions. Vahidkhah et al. [7] and Bailoor et al. [8] employed straight outflow extensions in their TAV simulations, while Singh-Gryzbon et al. [9] and Mayo et al. [10] utilized extensions extruded along the face normal of the segmented ascending aorta. In contrast, Brandon et al. [11] introduced a fixed length of 6 cm to the ascending aorta, creating approximately a 90-degree bend. It is worth noting that all of the aforementioned studies reported flow and hemodynamic indices in the vicinity of the TAV as part of their investigations.

In the studies mentioned above, Bailoor et al. [8] utilized a reduced degree of freedom (DOF) valve model for the FSI simulations to study the healthy and prosthetic aortic valves under differing stiffness values. Singh-Gryzbon et al. [9] utilized Reynolds-Averaged Navier–Stokes (RANS) approach using the shear-stress transport transitional (SST-Trans) model and simulated the two phases of the cardiac cycle (systole and diastole) as two separate simulations. Transient flow simulations were performed under laminar flow assumptions by Mayo et al. [10] for two valve-in valve configurations and Brandon et al. [11] modeled the flow under laminar assumptions with the leaflet motion prescribed by a porosity model. Large eddy simulations have been extensively applied arterial flows especially flows with transitional Reynolds numbers [12–14]. Other modeling approaches, such as Fluid-Structure Interaction (FSI), porosity and Discrete Particle Method (DPM)-based approaches, exist but may not be straightforward to implement when dealing with large deformation and contact dynamics.

From a numerical simulation standpoint, Direct Numerical Simulations (DNS)—in which all scales are resolved—prove to be more suitable for very low Reynolds numbers, where computational demands remain challenging. In our study, for instance, with a mean Reynolds number of 4500, the required mesh size for DNS would be on the order of  $9 \times 10^{10}$  grid points (the grid point requirement scales approximately with Reynolds number cubed), making the simulation nearly impractical. On the other end of the spectrum, RANS models are better suited for very high Reynolds numbers, where fluctuating components are implicitly represented through time-averaged flow fields. However, since arterial flows are pulsatile and not fully developed, RANS models are ill-suited as they were designed for simulating well-developed flows. Therefore, considering the comprehensive spatial and temporal aspects of our investigation, Large Eddy Simulation (LES) emerges as a pragmatic and well-suited intermediate approach. With

substantially lower computational demands than DNS, LES provides time-accurate information on both the large and sub-grid scales.

To explore the impact of modeling assumptions pertaining to anatomy, our study primarily focuses on the outflow from the aortic root housing the TAV. Specifically, we aim to investigate the effects of distal aortic arch anatomy on hemodynamic characteristics near the TAV site. For this purpose, we analyze three patient-specific anatomies with four different types of aortic arch configurations (totaling  $N = 12$  cases) under systolic conditions. The main objective of our research is to quantitatively evaluate the influence of distal aortic arch anatomy on hemodynamic characteristics in the vicinity of the TAV site.

## Materials and Methods

### Study Cohort

The study was performed under the limited data usage agreement between the Freiburg University Hospital and Georgia Institute of Technology, where the retrospective post-TAVR computed tomography angiography (CTA) data for 155 patients (mean age  $82.2 \pm 5.4$  years, 57% female) who underwent a balloon-expandable 23 mm SAPIEN 3 TAV (Edwards Lifesciences, Irvine, CA, USA [15]) implantation at the University Heart Center Freiburg-Bad Krozingen was anonymized and de-identified. The contrast-enhanced retrospective ECG-gated data acquisition of the aortic root was performed using a second-generation dual-source CT scanner (Somatom Definition Flash, Siemens Healthcare, Forchheim, Germany) with a temporal resolution of 75 ms. The examination involved administering a total of 40 mL of iodinated contrast agent (Imeron400<sup>®</sup>, Bracco, Konstanz, Germany) at a rate of 4 mL/s, followed by a saline bolus chaser of 40 mL at 4 mL/s. Data acquisition began 7 seconds after the attenuation of a region of interest placed in the left atrium reached 70 Hounsfield units, using the bolus tracking technique. The detailed description of the image acquisition for this cohort is described in Pache et al. [16]. Cardiac CTA data were reconstructed at either 5% or 50 ms steps throughout the cardiac cycle with a section thickness of 1 mm and an increment of 0.8 mm using a stent-specific convolution kernel. Written informed consent was obtained through the Institutional Review Board approved study “Extensive Hemodynamic Analysis of Transcatheter Heart Valve Imaging Data” (#H17256).

### Image Segmentation and Surface Geometry Extraction

The CTA images were segmented using 3D Slicer to obtain the 3D reconstructions of the patient-specific aortic root,

LVOT, coronary arteries, and the 23-mm SAPIEN 3 valve. The reconstructed root geometries were then smoothed to remove non-physiological artifacts. Due to the lack of sufficient resolution to capture the SAPIEN 3 valve, a high-resolution stent was obtained from  $\mu$ CT images (Siemens Medical Solutions USA, Inc., Malvern, PA). The stent placement was then matched to the patient CT. The TAV leaflets were defined using the parametric leaflet model described by Xu et al. [17]. Due to the unavailability of the native leaflet information, the leaflets were geometrically represented by a uniform cylindrical structure as described in Singh-Gryzbom et al. [9].

### Development of Patient-Specific Models

We selected three patients from the overall cohort for our study. Figure 1 illustrates the segmented root anatomies of these patients, including the TAV and its subparts used in the simulation. The patient selection aimed to include three distinct anatomical features that we hypothesized could have an impact on the flow dynamics within the aortic root, specifically up to the sino-tubular junction. As a result, we chose one case, C1, with hypo-attenuated leaflet thickening (HALT +ve), a growing concern where the leaflet motion is reduced following TAVR, the second case, C2, with a proximal aortic arch below the population-averaged angulation, therefore a shorter bend radius, and the third patient, C3, without HALT i.e., HALT -ve.

The segmented patient aortic root anatomies were augmented with four different types of outflow extensions, as illustrated in the bottom half of Fig. 1. The first type, denoted as  $Cn_{90^\circ}$  bend, was generated by extruding the anatomy to form a right-angled bend at  $90^\circ$ , commonly used in “*in-vitro*” casted models and also in numerical simulations. In the second type,  $Cn_{full}$ , the complete descending aorta was reconstructed using morphological data on healthy aortic arches provided by Boufi et al. [18]. The data provided detailed measurements, including aortic angulations ( $\theta_{Z0} - \theta_{Z3}$ ), which were utilized to determine an idealized centerline of a healthy descending aorta. The idealized centerline was then aligned with the anatomical centerline of the segmented aortic root anatomies, and then extruded, thus mimicking an idealized descending aortic arch. The third type,  $Cn_{part}$ , represented a truncated subset of the previously mentioned configuration, where the descending aorta was partially clipped. With this configuration, we aimed to investigate the necessity of the full length of the descending aorta. Finally, the fourth type,  $Cn_{norm}$ , was generated by extruding the anatomy in the direction along the normal vector of the segmented outlet patch. Each of these flow extensions had a length of at least 6 times the diameter of the annulus ( $D$ ). The inflow extensions of all the models extended along the face of the inlet patch of the segmented anatomy up to  $6D$ .

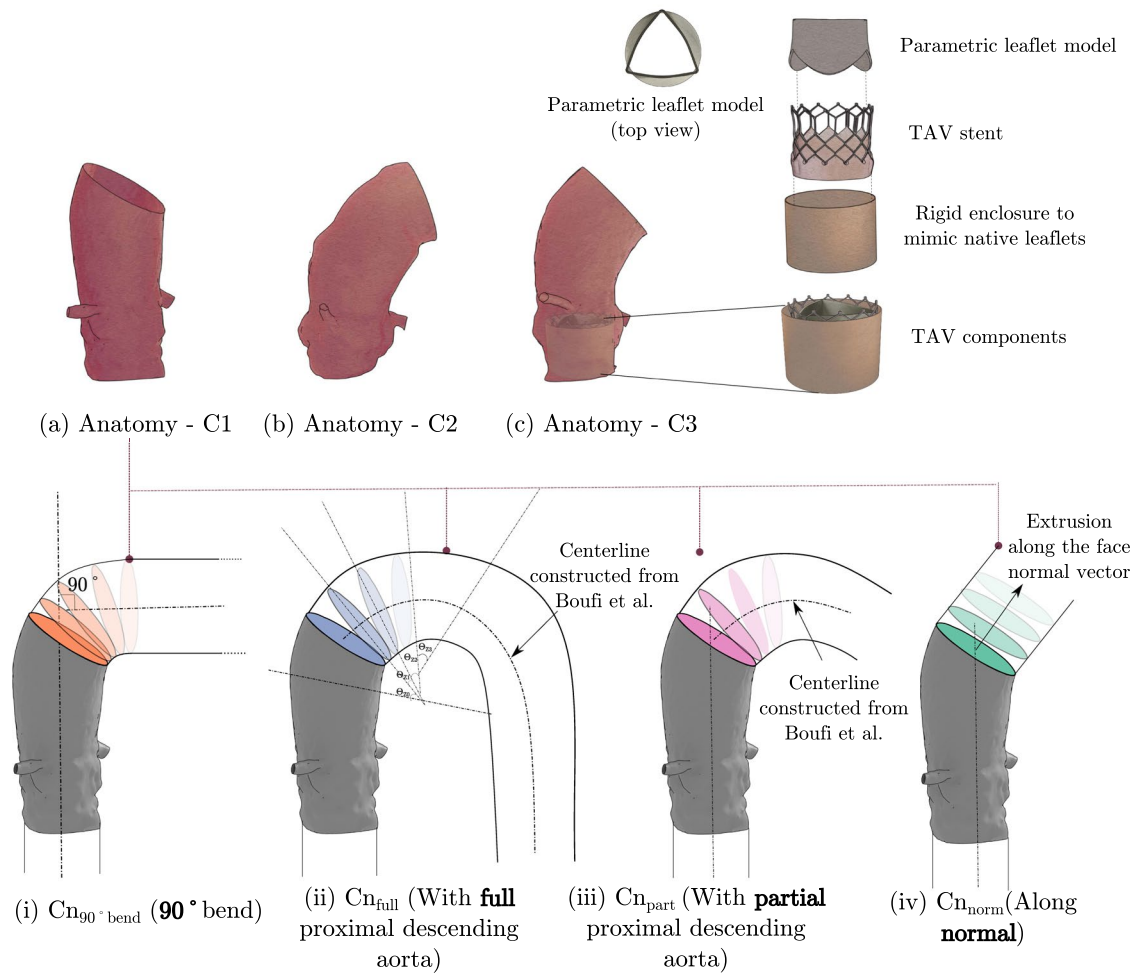


**Fig. 1** Top: The aortic root anatomies for the three cases after reconstruction and smoothing, along with the subparts of the TAV in an exploded view. Bottom: The four configurations that were constructed for each anatomy

### Numerical Methodology

#### Governing Equations

Blood in larger vessels can be effectively modeled as a Newtonian fluid, as non-Newtonian effects tend to become negligible under the high stresses encountered in large vessels, such as those considered in the present study. Consequently, the flow characteristics can be aptly described by the unsteady, viscous, and incompressible Navier-Stokes equations in their filtered form, as given as,

$$\frac{\partial \bar{u}_i}{\partial x_i} = 0, \tag{1}$$

$$\frac{\partial \bar{u}_i}{\partial t} + \frac{\partial (\bar{u}_i \bar{u}_j)}{\partial x_j} = -\frac{1}{\rho} \frac{\partial \bar{p}}{\partial x_i} + \nu \frac{\partial}{\partial x_j} \left( \frac{\partial \bar{u}_i}{\partial x_j} + \frac{\partial \bar{u}_j}{\partial x_i} \right) - \frac{\partial \tau_{ij}}{\partial x_j} \tag{2}$$

for which the closure is provided with a suitable sub-grid scale (SGS) model. The main function of the sub-grid scale model is to extract the energy from the resolved large eddies to resemble the dissipation of energy cascade. Several forms of these sub-grid scale models exist. However, a large majority of them are based on the RANS counterparts which rely on the eddy viscosity hypothesis. The Smagorinsky model approximates the SGS stress as,

$$\tau_{ij} - \frac{1}{3} \delta_{ij} \tau_{kk} = 2C_s \Delta^2 |\bar{S}| \bar{S}_{ij} \tag{3}$$

where  $\delta_{ij}$  is the Kronecker delta function. The sub-grid scale eddy-viscosity is given as  $\nu_t = (C_s \Delta)^2 |\bar{S}|$  where  $C_s$  is the Smagorinsky constant that ranges between 0.18 and 0.23;  $\Delta$ , the filter width governed by the mesh size ( $\Delta = (\Delta V)^{\frac{1}{3}}$ ) and the magnitude of the strain rate tensor,  $|\bar{S}| = (2(\bar{S}_{ij} \bar{S}_{ij}))^{1/2}$ ,  $\bar{S}_{ij}$  is the rate of strain tensor of the resolved velocity field where  $\bar{S}_{ij} = (\partial u_i / \partial x_j + \partial u_j / \partial x_i) / 2$ .

Although this model has been successfully used, a particular drawback is the constant value for  $C_s$ . In certain flow conditions where high shear occurs, the value of  $C_s$  must be decreased and needs to be countered using a damping function. Although this is beneficial, the value of the constant must be dependent on the local flow properties hence dynamically computed rather than restricting it to one value. Germano et al. [19] proposed these changes for the dynamic computation of the Smagorinsky constant  $C_s$  which was later remedied by the error minimization using the least-squares method by Lilly [20]. This modified version of the dynamic Smagorinsky model is employed in the current research.

### Solver, Spatial and Temporal Discretization

The simulations were conducted using LES with the Open Field Operation and Manipulation (OpenFOAM) code. A second-order accurate backward implicit scheme was employed for time discretization. The convection terms were discretized using a second-order accurate central differencing scheme. The pressure-velocity coupling was resolved using the PISO-SIMPLE (PIMPLE) algorithm, which combines the Pressure Implicit with Splitting of Operator (PISO) algorithm and the Semi-Implicit Method for Pressure-Linked Equations (SIMPLE) algorithm. This coupling allows for the iterative calculation of pressure on a mesh from velocity components by coupling the Navier–Stokes equations. The code was parallelized using the Message Passing Interface (MPI) protocol, and the graph partitioning algorithm SCOTCH [21] was utilized to decompose the solution domain into the necessary number of sub-domains for parallel computing. The simulations were performed on Linux machines equipped with dual Intel Xeon 6226 @ 2.7 GHz CPUs on the PACE Phoenix cluster [22]. On average, each simulation (covering 5 flow cycles) took approximately 6 hours of CPU time using 28 parallel processors.

Mesh sensitivity analysis was performed (level one refinement) for the case with the highest flow rate ( $C2_{norm}$ ) and then was doubled (level two refinement) to compare the velocity-time traces in the shear layer of the antegrade jet. The accuracy of LES tends to approach that of DNS as spatial resolution increases and filter width (i.e., implicitly, the discretization volume) decreases. As a result, in this study, we aim to explore the appropriate levels of mesh resolution required for the present configuration. The difference in results between level one and level two refined meshes was less than 2%. To err on the side of caution, all the level one meshes were increased by a factor of 1.5 and used for the final simulations. The grid discretization parameters are given in Table 1. All the grids were discretized with hexahedral control volumes and were generated with the native OpenFOAM mesh utilities “*blockMesh*” and “*snapHexMesh*”. Special attention was given to clustering cells

around the regions of the stent frame and the bioprosthetic leaflets to achieve additional refinement and adequately resolve the flow around these relatively thin structures. The meshing process occurs in two steps in cases involving complex shapes, such as an aortic root with a TAV. Initially, a background hexahedral mesh was created to bound the entire model. Subsequently, in the second stage, the background mesh was adjusted to conform to the detailed structures outlined by the STL files obtained through segmentation. The refinement levels were controlled for each component, including the stent frame and prosthetic leaflets, allowing for a balance between detail and computational efficiency. For instance, starting with a non-dimensional cell size of 1 on the background mesh, a level one refinement reduced it to 0.5, and a level two refinement further reduced it to 0.25. For our current study, two levels of refinement were employed for the stent frames and the prosthetic leaflets for all the models. Figure 2a shows an overview of a surface mesh (case C1) with the inset showing a clipped plane to demonstrate the hexahedral meshes near the vicinity of the TAV.

### Boundary Conditions, Fluid Properties and Solution Control

Simulations were configured and run with a fully open configuration for the systolic interval and from here on one flow cycle refers to this systolic interval of 350 msec. Figure 2b shows the aortic flow rate waveform imposed at the inlets along with the generic pressure waveform at the outlet similar to that of Singh-Gryzbon et al. [9]. A flat velocity profile was imposed allowing the flow to develop naturally. For each patient, the aortic flow waveform was scaled to match the patient’s peak systolic flow rate, obtained from analysis of the left ventricular volume over the cardiac cycle. As patient-specific coronary flow data were not available for this cohort, total coronary flow was assumed to be 5% of the patient’s cardiac output with a 60/40 split to the left coronary artery (LCA) and right coronary artery (RCA), respectively. All structures were assumed to be rigid and non-permeable, and a no-slip boundary condition was applied to the walls. Blood was assumed to be Newtonian with a kinematic viscosity and density of 0.0036 Pa s and 1060 Kg/m<sup>3</sup>, respectively. All simulations were run for 5 cycles to damp initial transients and data from the last cycle is used, with 7000 time-steps per cycle or a temporal resolution of 0.05 msec given the imposed period of 350 msec. This criterion was sufficient to keep the Courant-Friedreich-Lewy (CFL) number below 1.0 at all times. Although numerical stability in implicit solvers is not directly tied to a specific Courant number limit, we emphasize the importance of maintaining a CFL number below one, as larger time steps, while feasible, may compromise simulation accuracy and convergence

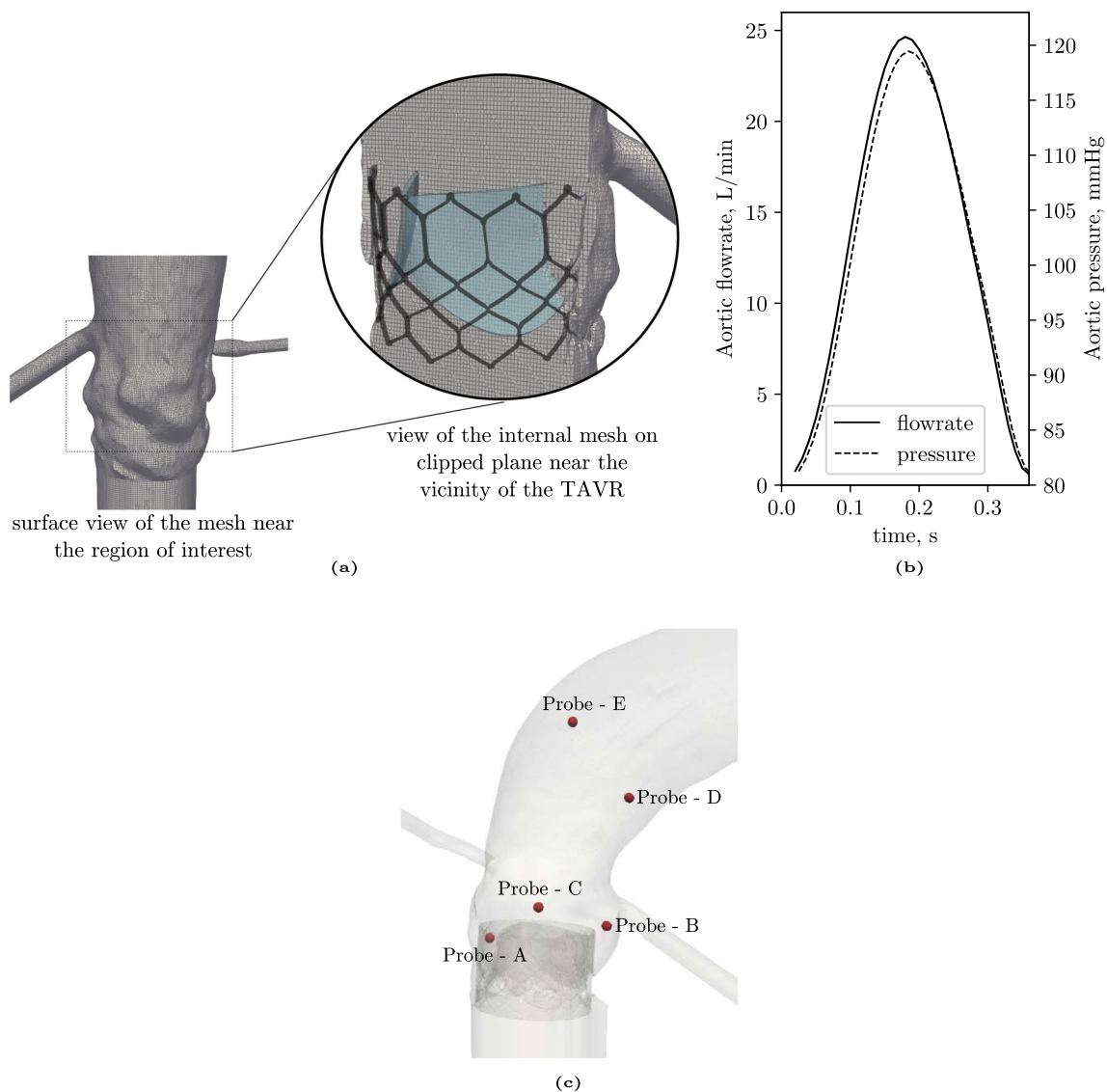


**Fig. 2** **a** Overview of the surface mesh and the inset showing a close-up view of the internal hexahedral mesh discretization with the TAVR overlaid for comprehension. **b** Aortic flow waveform and aortic

pressure waveform used as boundary conditions and **c** illustration of digital probe locations within the anatomy

when excessively large. Velocity and pressure data were saved in equally spaced time points for post-processing.

### Spectrograms, Washout Curves and Mesh Flattening

To investigate the temporal evolution of flow frequencies in the domain, spectrograms were generated following the methodology described in Natarajan et al. [23]. The spectrograms were constructed by averaging the power spectra obtained from the short-time Fourier transform (STFT) analysis of the cell-centered velocity-time data within the region of interest. The percentage overlap is crucial in determining the additional spectral frames between two non-overlapping windows. A 75% overlap was selected as

it strikes a reasonable compromise between spectral resolution and smearing. For our case, aiming for 10 non-overlapping windows from 3500 snapshots translates to 350 samples, and choosing the nearest power of 2 yields 256. With a 75% overlap, i.e., 3 additional windows between two non-overlapping windows, yielding 36 windows. This configuration results in a frequency resolution of 13 Hz and a temporal resolution of 0.0001 seconds. Given our focus being on the TAV, we specifically choose our region of interest centered around the TAV. This region encompasses all nodal points within a spherical clipping of radius  $2D$ , where the sphere's center aligns with the center of the TAV. For each model, STFT spectrograms were generated using approximately 20,000 data points

**Table 1** Anatomical measurements, flow rates and grid information for the cases investigated

Anatomy	Age (years)	Peak systolic flowrate (L/min)	$D_{LVOT}$ (mm)	$D_{AA}$ (mm)	$D_{annulus}$ (mm)	$D_{sinus}$ (mm)	No. of cells ( $\times 10^6$ )
Case - C1	93	23.1	23.8	30.4	23.0	25.8	
(i) 90° bend							3.03
(ii) Full Proximal descending aorta							6.60
(iii) Partial proximal descending aorta							4.90
(iv) Extrusion along normal							2.91
Case - C2	84	33.9	18.8	39.1	20.5	30.6	
(i) 90° bend							3.08
(ii) Full Proximal descending aorta							7.20
(iii) Partial proximal descending aorta							5.45
(iv) Extrusion along normal							3.15
Case - C3	93	23.1	23.8	30.4	23.0	25.8	
(i) 90° bend							2.90
(ii) Full Proximal descending aorta							4.50
(iii) Partial proximal descending aorta							3.36
(iv) Extrusion along normal							3.60

within the region of interest (sphere of radius  $2D$  centered at the TAV), and 3,500 equally spaced time steps over the flow cycle were considered.

Flow stasis has been hypothesized to contribute to HALT and therefore it is imperative to assess the washout characteristics (which can be surrogate for flow stasis measurement). Washout curves typically show the percentage ratio of fluid particles remaining from the initially seeded in the sinus/neo-sinus region at the onset of the flow cycle as a function of time. Steep washout curves, where more particles exit the domain in fewer cycles, generally indicate better flow circulation. For this study, approximately 20,000 massless particles were seeded with a maximum inscribed sphere of particles at the center of the TAV with a diameter equivalent to the annulus such that the particles clustered around the TAV site. The particles were tracked over the last three flow cycles, and the percentage remaining as a function of time.

The impact of the flow on the aortic wall are characterized through Time Averaged Wall Shear Stress (TAWSS) and Oscillatory Shear Index (OSI) where TAWSS is defined as

$$TAWSS = \frac{1}{T} \int_0^T |\tau_w| dt \quad (4)$$

and OSI given by

$$OSI = \frac{1}{2} \left[ 1 - \frac{|\int_0^T \tau_w dt|}{\int_0^T |\tau_w| dt} \right] \quad (5)$$

where  $\tau_w$  is the wall shear stress and  $T$  corresponds to the duration of one flow cycle.

Due to the complex geometry of the anatomies considered in this study, visualizing hemodynamic indices from a single view vector can result in occlusion and difficulty in interpretation. To address this, mesh parameterization and mesh flattening techniques are employed, allowing for the visualization of the 3D geometry on a 2D plane through a bijective mapping between the two surfaces. Figure 3 illustrates the mesh parameterization technique used in the current study. For the anatomies considered here, the surfaces are triangulated and flattened using a least squares conformal mapping (LSCM) that minimizes angular distortion [24]. To enable the bijective mapping between the 3D and the “unwrapped” 2D surface, the index order is preserved. For clarity, the RCA and LCA branches are clipped, and the maps focus on the ascending aorta. This allows for a clearer representation of the hemodynamic indices on the flattened surface. For more information on the flattening techniques particularly for medical visualizations, the reader may refer to the work of Kreiser et al. [25].

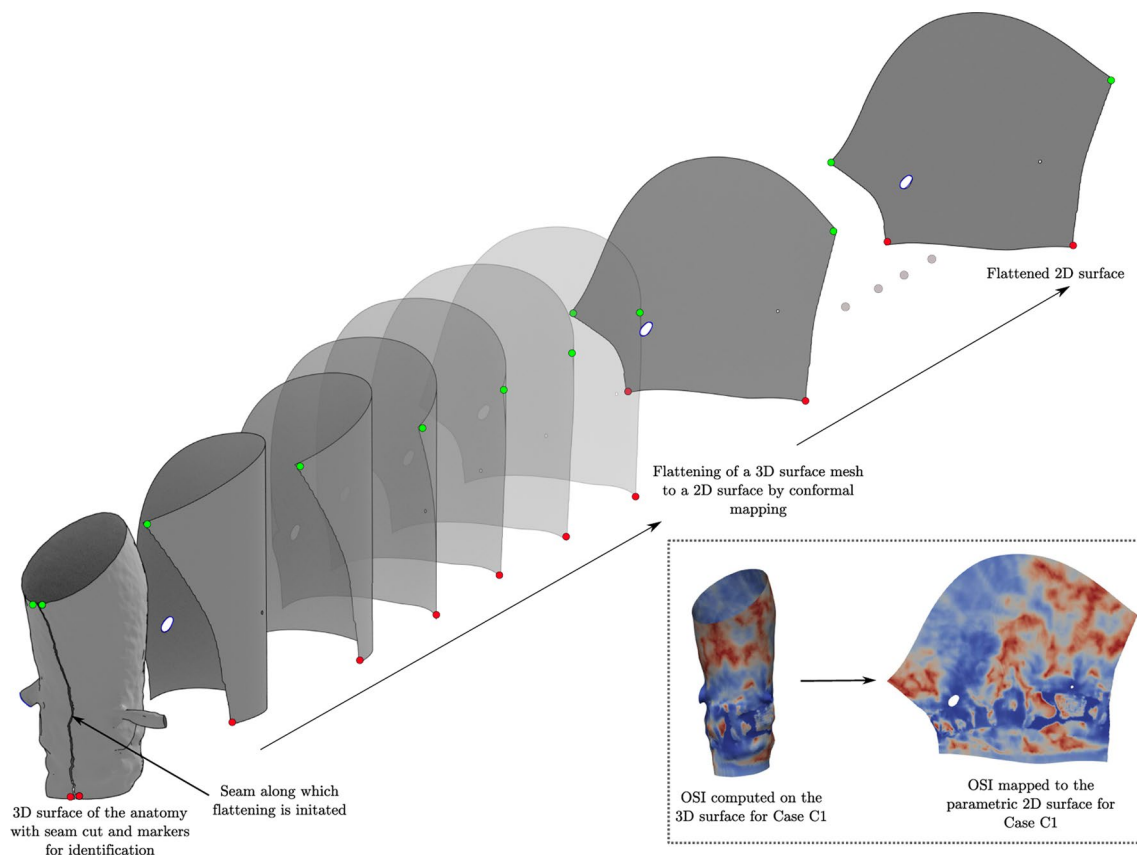


**Fig. 3** Illustration of mesh parameterization where a 3D surface (C1) is ‘unwrapped’ to a 2D surface. The bottom figure shows instantaneous WSS on a 3D surface where the data is occluded to the viewer and the corresponding 2D surface where all the data is free of occlusion

## Results

Figures 4, 5 and 6 (a–e) show the instantaneous velocity vs. time traces for the last flow cycle at selected probe points in the three aortic root anatomies and their ascending aorta, and their respective distal configurations. To ensure spatial consistency, the probe locations were maintained across the patient anatomies as follows: point A in the neo-sinus (space between the native and bioprosthetic leaflets), point B in the anatomic sinus (space between native leaflets and aortic wall), point C on the centerline of the jet, point D at the inner bend near the end of the proximal ascending aorta, and point E near the outer bend (i.e., the end of the distal ascending aorta) and are illustrated in Fig. 2c. The figures (f–j) show the corresponding power spectral density (PSD) curves derived from their respective velocity data.

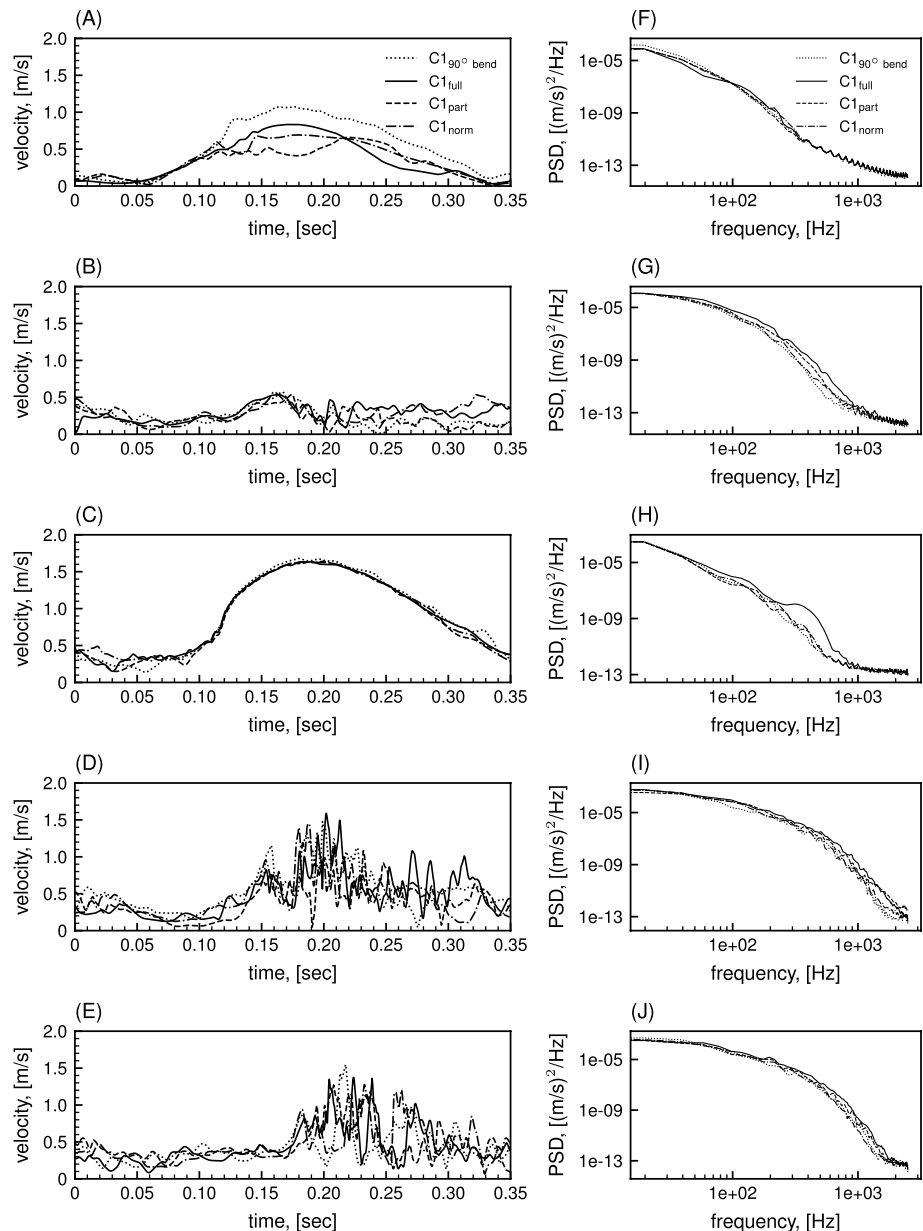
Minor variations in velocity magnitude can be observed within each group of the three cases (see supplemental animation 1 for Case 3). The most significant differences are observed in the velocities obtained at the neo-sinus, both within their subgroups and across cases. However, the overall trend is consistent across all the tested models for a given probe location. This trend adherence is also reflected in the

PSD plots, where all cases exhibit a monotonic decrease in power with increasing frequency. The flow frequencies in this case are a measure of complex flow patterns and their modulation and evolution in time are often difficult to discern through point-wise measurements especially since the aortic arch, including the ascending and the descending regions, are known to present complex flow structures and have been reported by several studies.

Previous cardiovascular studies have reported flow frequencies up to 100s of Hz (Chnafa et al. [12] for the heart, Bozetto et al. [26] for arteriovenous fistulae, Mancini et al. [27] for carotid stenosis and Valen-Sendstad et al. [28] for aneurysms). Figure 7 shows the averaged spectrograms computed for all the cases investigated. As expected, all the spectrograms exhibited broadband frequencies up to 1250 Hz. The peak frequencies in the spectrograms were observed around peak systole and persisted for a brief period ( $\approx \Delta t$  of 0.15 s) and then eventually lost momentum to relaminarize into lower frequency bands towards the end of the flow cycle. The sensitivity of the gross flow frequencies to the type of distal aortic arch type was found to be minimal in the cases examined.



**Fig. 4** Instantaneous velocity obtained for C1 from probes located at **a** neo-sinus, **b** sinus, **c** antegrade jet, **d** inner bend, **e** outer bend, and the figures **f-j** showing their corresponding power spectral density (PSD)



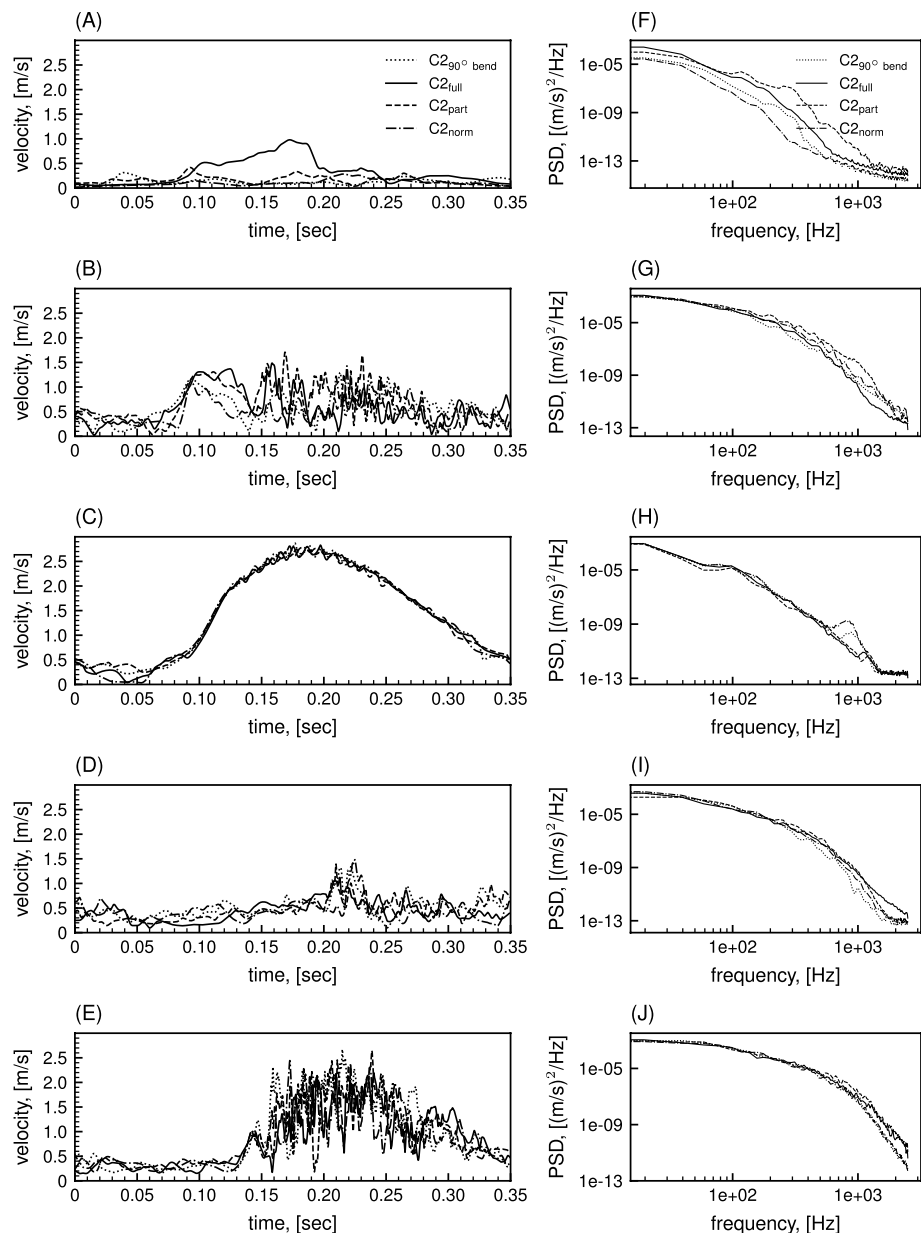
To further investigate the flow phenotypes, instantaneous flow structures at peak systole were visualized with  $Q$ -criterion [29] and shown in Fig. 8 for all the models. The flow structures were extracted using a uniform isovalue across all models. While significant differences were observed in the outflow extension regions, the flow structures within the region of interest, namely the aortic root, proximal, and distal ascending aorta, appeared largely unaffected. The larger flow structures, resembling hairpin-like structures, were well-preserved across all the models, gradually breaking down into smaller structures as they propagated through the aortic arch. Though these characteristics change with the leaflet motion, the

aim however is to assess the change in local flow dynamics and therefore could still be a useful metric for rigid simulations.

Figure 9 (and supplemental animation 2) show the washout characteristics of the models. Across all the models examined, it can be observed that nearly 90% of the particles are washed out by the end of the first flow cycle. Subsequently, an additional 5% of particles are washed out towards the end of the second cycle, and nearly all the particles are completely washed out by the end of the third flow cycle.

Pressure gradients are shown in Fig. 10 along the centerline of the models during peak systole as they often are

**Fig. 5** Instantaneous velocity obtained for C2 from probes located at **a** neo-sinus, **b** sinus, **c** antegrade jet, **d** inner bend, **e** outer bend, and the figures **f–j** showing their corresponding power spectral density (PSD)

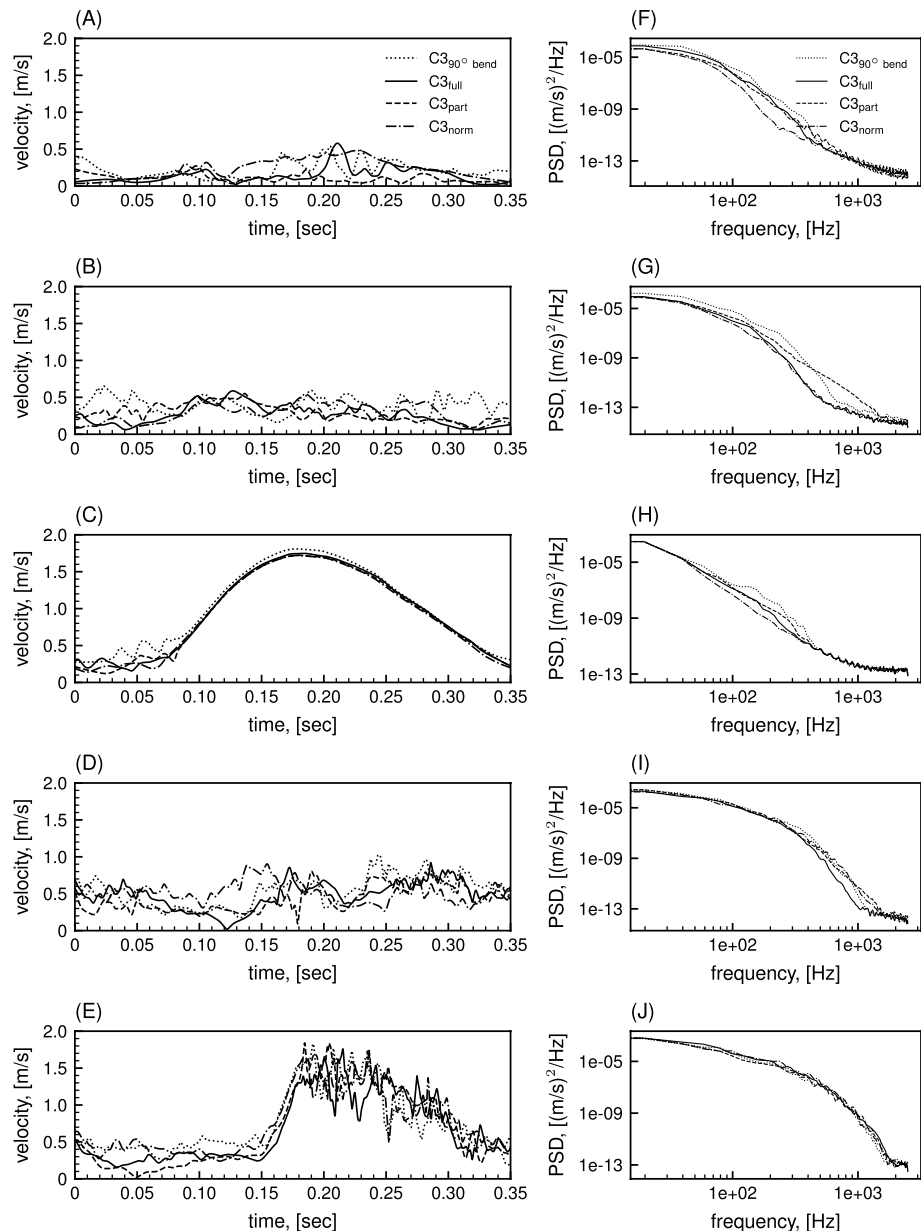


used to evaluate the performance of the TAV. The plot shows the gradients along the regions of the TAV, the segmented root model, and the added flow extensions. The corresponding boundaries are indicated by vertical dashed lines. The annulus pressure was obtained at the centerline precisely where the TAV base is positioned. In cases C1 and C3, where models feature a 90-degree bend, there is a slight elevation in pressure drop, followed by a longer recovery time. Conversely, in case C2, (selected due to its anatomical characteristics) where the proximal aortic arch exhibits a notably short length, the pressure drop is relatively higher. The overall trend again is intact where there is a drop in pressure owing to the TAV and eventually recover

downstream approximately around the region where the flow extensions begin.

Figure 11 presents the mapping of TAWSS onto the parameterized 2D surfaces for all the models. A distinct difference is observed between case C2 and cases C1 and C3. In case C2, which features a relatively shorter bend radius, the local TAWSS is more pronounced in the impingement zones. This can be attributed to the antegrade jet impacting the wall with minimal loss in momentum. The observed range of TAWSS values aligns with findings from previous studies focusing on the aorta. However, there is minimal variation observed between different configurations within each anatomical subtypes. This suggests that the specific configuration of the TAV and the added flow extensions do

**Fig. 6** Instantaneous velocity obtained for C3 from probes located at **a** neo-sinus, **b** sinus, **c** antegrade jet, **d** inner bend, **e** outer bend, and the figures **f–j** showing their corresponding power spectral density (PSD)



not significantly affect the TAWSS distribution along the ascending aorta.

A similar trend is observed in the distribution of OSI (shown in Fig. 12), where regions of low OSI along the ascending aorta (indicative of highly unidirectional flow) coincide with the impingement regions of the jet. This further supports the notion that the flow patterns and hemodynamic indices are influenced by the impact of the jet on the aortic wall.

## Discussion

Using LES, for three anatomies and four types of representative distal aortic arch anatomies, our findings suggest that under the given configuration and boundary conditions, resulted in significant, albeit generally not substantial, differences in flow and hemodynamics in the vicinity of the TAV. Both qualitative and quantitative assessments showed that the impact of the type of extension used has a modest impact on the TAV hemodynamics investigated herein.

Instantaneous flow statistics show that the overall trends are preserved within the groups and their corresponding transformations to the frequency domain showed a monotonic decrease in power with frequency as expected. A

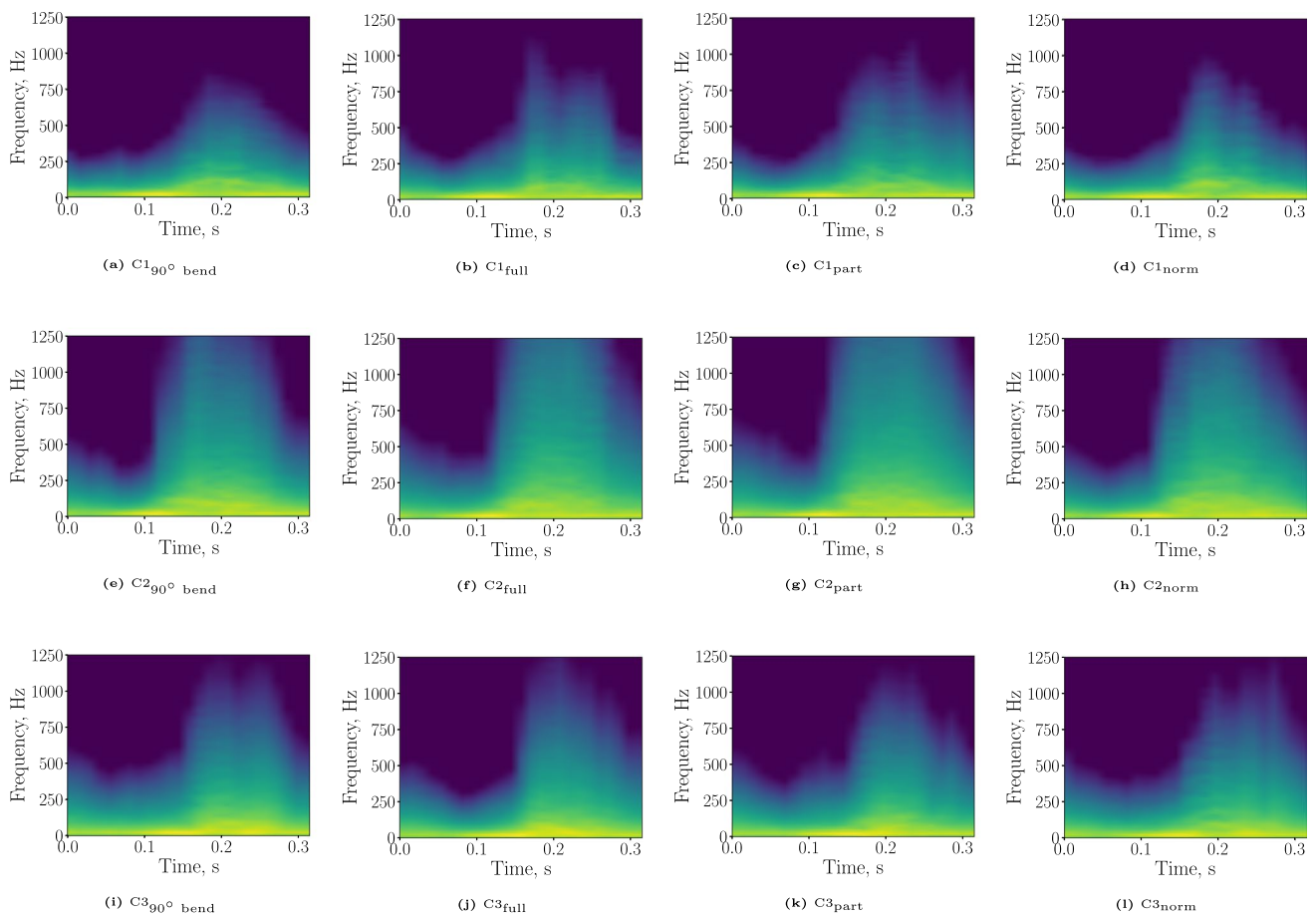


**Fig. 7** Aortic root averaged spectrograms of flow velocity for cases C1, C2, C3 and their corresponding sub-configurations. In the spectrograms, yellow represents a high level of power and dark blue represents lower power

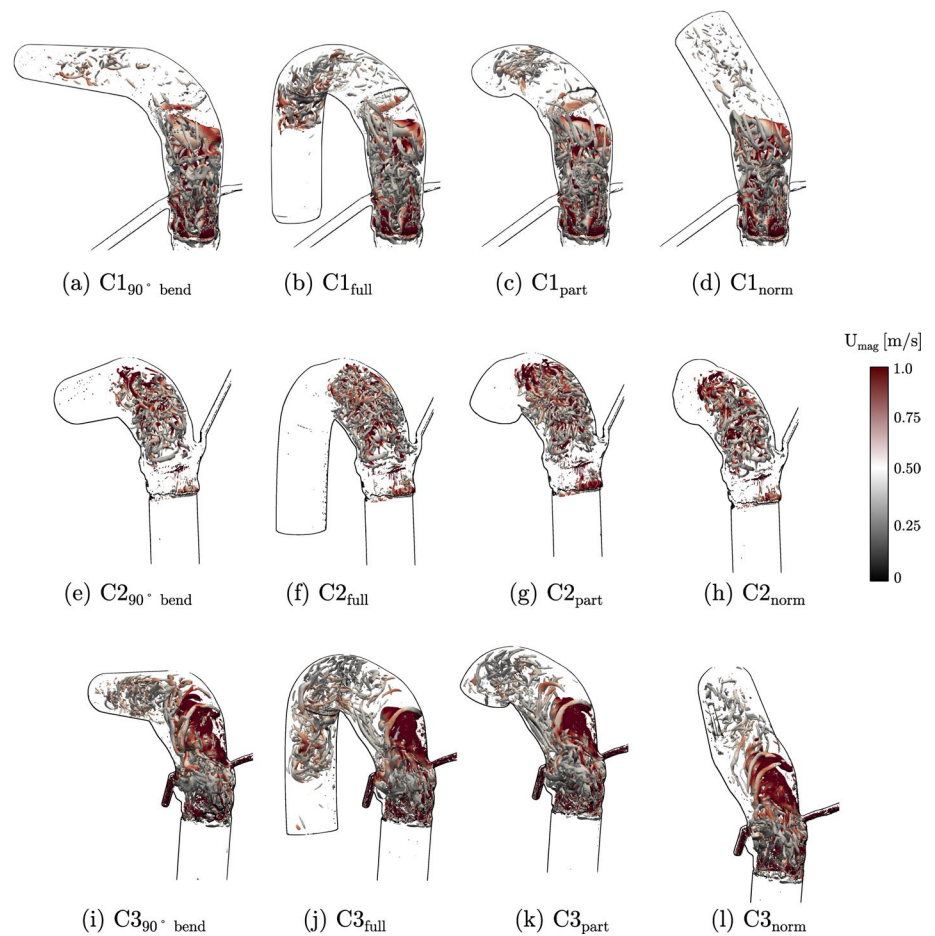
closer look at the power spectral power showed (for case C3) that  $C3_{90^\circ\text{bend}}$  showed marginally higher power than its counterparts however this was not observed in other anatomies. Owing to the spatial heterogeneity of the flows, it was imperative to not only observe the point-wise measurements, but also the global behavior of the flow. In an attempt to capture any changes to the global flow instabilities induced by the distal aortic arch anatomies, averaged spectrograms were used. Spectrograms were constructed to understand the temporal evolution of the flow fluctuations within the sub-groups across of the three patient-specific anatomies.

In the context of vascular pathology, the influence of high-frequency flow fluctuations on degenerative changes, such as endothelial or mural cell remodeling and turnover, has been well-documented [30–32]. While point wise measurements of these flow fluctuations provide valuable insights, they often lack the temporal information, needing additional information for a comprehensive understanding of the flow phenotype. Spectrograms serve as a concise representation of flow fluctuations, offering a means to capture their temporal dynamics. Manprin et al. [33] employed ECG

signals and a recurrent neural network to predict conduction defects post TAV implantation, utilizing spectrograms to extract features based on spectral content. However, their analysis was limited to frequencies up to 500 Hz. Given the relevance of high-frequency flow fluctuations in degenerative changes, it becomes imperative to extend investigations above this frequency range. Again, no substantial differences were observed at frequency ranges, perhaps even up to 250 Hz. Marginal differences are observed at the peaks i.e., high frequencies but no apparent changes to the gross flow features were seen. In patient-specific modeling for TAVRs, spectrograms can be a useful short hand representation of the overall flow field within a cardiac cycle. By elucidating the spectral content and temporal evolution, spectrograms can be a useful tool to provide a rich assessment on potential links to degenerative changes within the TAV or its vicinity.

The flow features in the form of  $Q$ -criterion iso-surfaces shown at peak systole indicate that in all the models, the broad features of the jet including the core antegrade flow, and the shear regions in the form of eddies are well preserved. Studies by Biasseti et al. [34] and Naim et al. [35]

**Fig. 8** Overview of the configurations showing vortex cores (3D isosurfaces of  $Q$ -criterion  $= 12.4 \times 10^3 \text{ s}^{-1}$ ) at peak systole colored by velocity magnitude



emphasize the significance of vortical structures and their interaction with the vessel wall or lumen. The findings suggest that higher-intensity vortex cores, particularly associated with maximum WSS, could potentially hint at the development and progression of thrombosis. While establishing a definitive association between vortex cores, WSS, and thrombus formation would require a more elaborate study and a larger cohort, the present results from our study demonstrate that this metric is relevant and could have clinical implications. Although significant differences in the flow features are observed in the models with descending aortic arches, the region around the TAV seems to be largely consistent. The dynamic bulk flow features remain intact irrespective of the distal aortic arch anatomy.

Alternatively, flow-stasis or regions with stagnant flow as opposed to dynamic flow were also studied as these markers have correlated to pathologies including subclinical leaflet thrombosis or leaflet thickening [7, 36–38]. The washout characteristics of the sinus/neo-sinus region have been used as a popular surrogate for measuring the flow stasis. The particles tracked over the last three cycles nearly collapse on each other illustrating that the sinus/neo-sinus hemodynamics are quite similar in all subgroups compared. While the

cases involving a 90-degree bend ( $C_{n_{90^\circ \text{ bend}}}$ ) demonstrated a marginal increase in slope, the disparity is practically insignificant.

The pressure gradient and recovery have been extensively characterized and are known to be dependent on several anatomical parameters including the valve area, sinus of Valsalva, and the ascending aorta [39], and can be used to optimize the valve hemodynamic performance. The trends observed in our current study are similar to that of the experimental studies of Samaee et al. [40]. Although the current simulations employ rigid configurations of the TAV, the distal aortic arch configuration may have an effect and alter the flow dynamics. Case C2 has a higher pressure drop possibly due to the inviscid effects dominating because of the relatively high peak systolic flow rate i.e., 33.9 L/min for C2 vs. 23 L/min for C1 and C3 (nearly 1.5 times higher). In the case where the bend occurs in close proximity to the aortic root, the pressure drop is significantly higher, and the impact of the root anatomy outweighs the effects of the extension type or distal arch anatomy at least for the obtained pressure gradient.

In the context of TAV studies, errors introduced by assumed distal anatomies can lead to variability in a subset

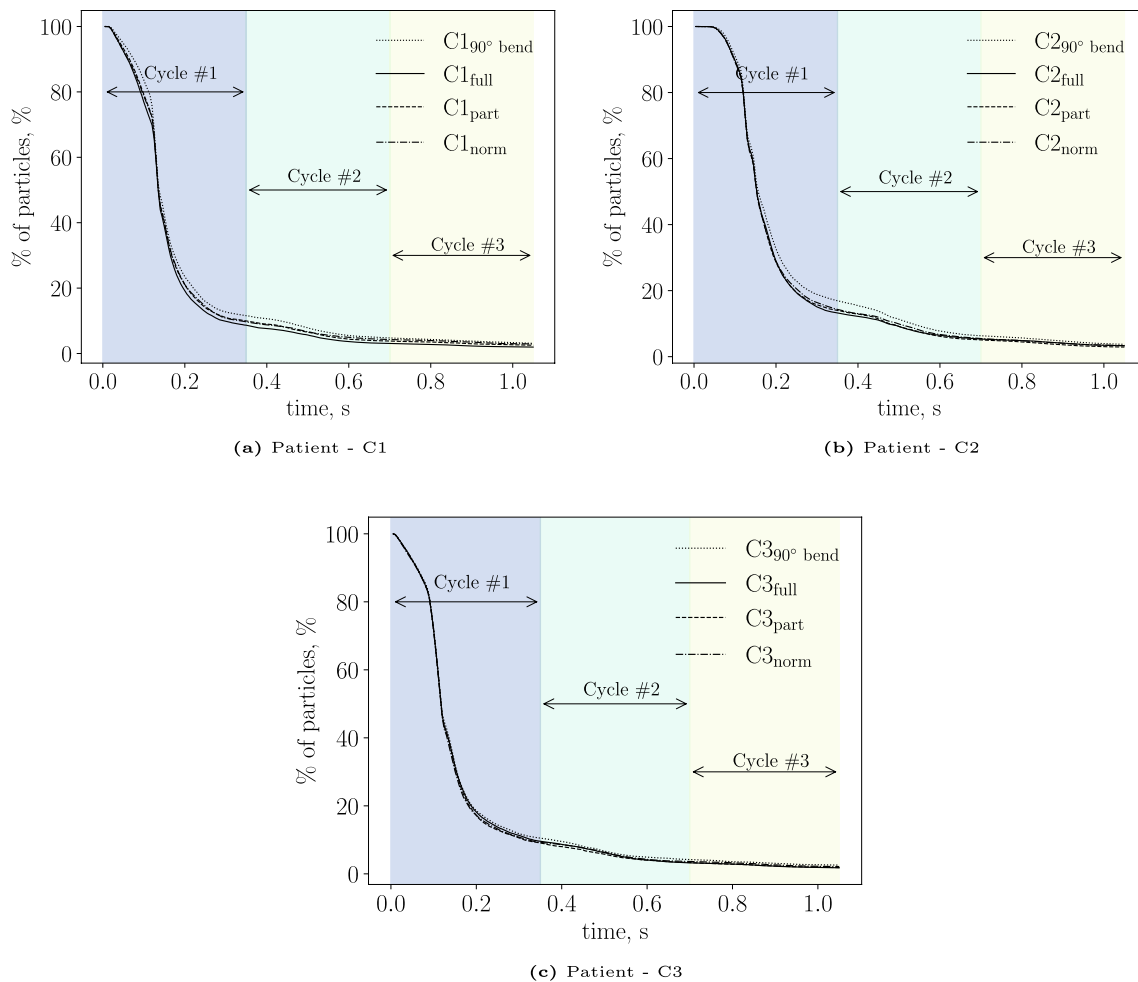


**Fig. 9** Washout curves for the models over the last three cycles

of cases. However, as the current study establishes, when the focus of the study is on the hemodynamics near the TAV, researchers can confidently adopt different flow extension approaches, allowing for comparisons between various research findings. While flow extension analysis plays a crucial role in improving patient-specific hemodynamic modeling of TAVs, it is also important to consider possible cost-benefit implications, particularly in terms of computational time. Nonetheless, factors such as solution accuracy and grid independence should not be compromised.

### Potential Limitations

In an attempt to understand the sensitivity of flow dynamics to the distal aortic arches alone, the study makes a few assumptions to understand its isolated effect. Fluid-structure interaction simulations would provide a more accurate evaluation of the kinematics however, we believe even for FSI simulations a study such as the one presented herein would be necessary to eliminate uncertainties on the effects of the

outflow configurations. The exclusion of supra-aortic vessels is another complication that needs to be addressed but is not straightforward because again the lack of imaging data and the need to register anatomies even if they were available or arrive at averaged anatomies and flow rate splits which in itself is broader study. The study is also restricted to one phase of the cardiac cycle i.e., the systolic phase and inclusion of the diastolic phase could potentially be a larger study. The study also assumed the parametric leaflet model under fully open condition. A more accurate way to represent the prosthetic leaflets would be from the post-imaging data, of course, assuming the resolution permits.

### Conclusion

The computational modeling of TAV simulations is prone to numerous sources of error and uncertainty. While it may not be feasible to address all these issues simultaneously, our focus in this study was on addressing one of the key

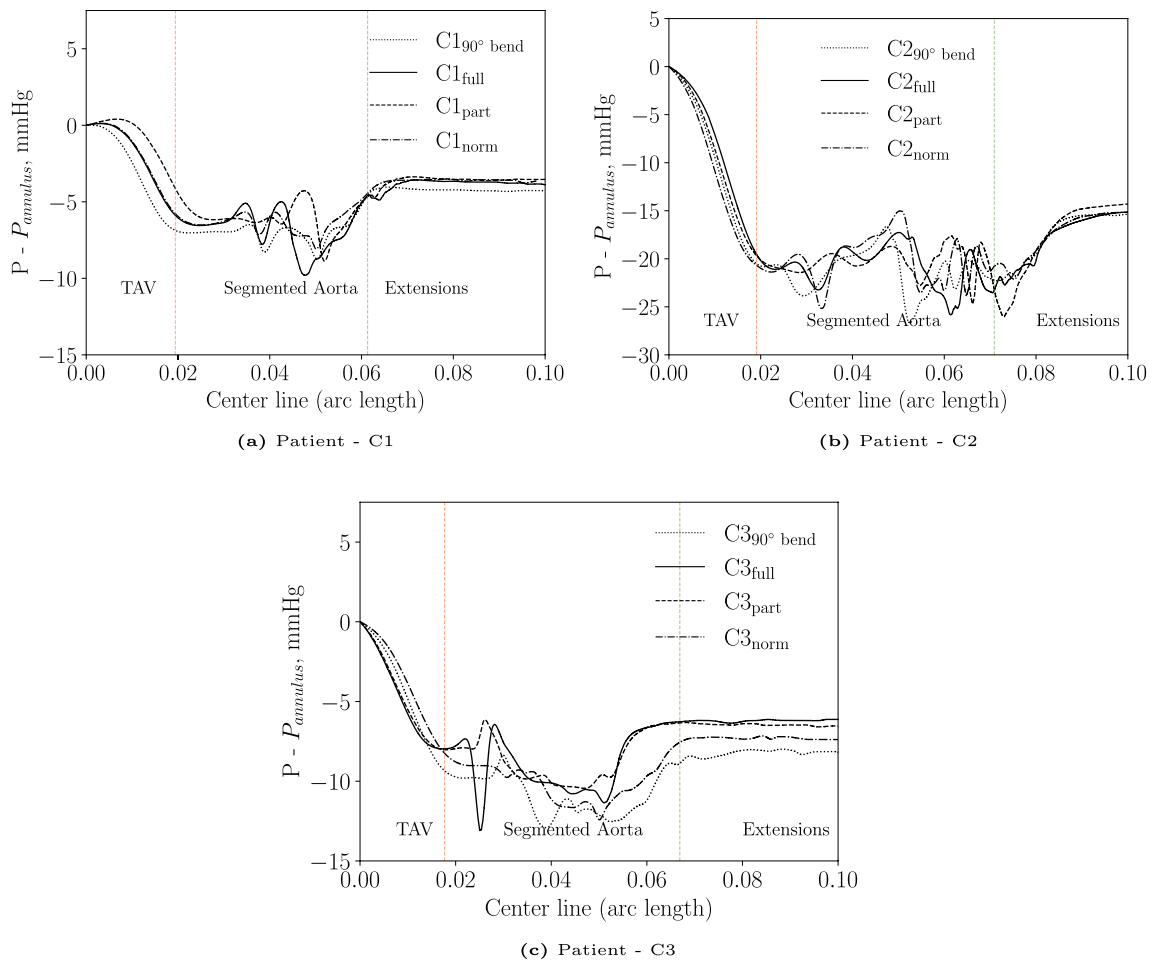


Fig. 10 Pressure gradient along the centerline for the models

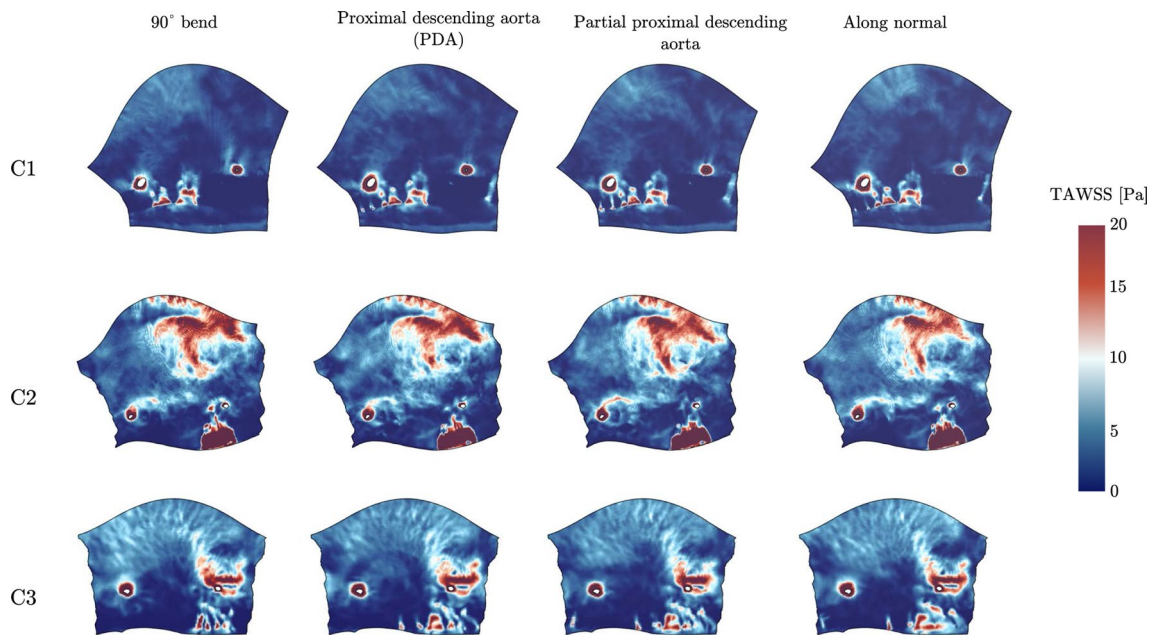
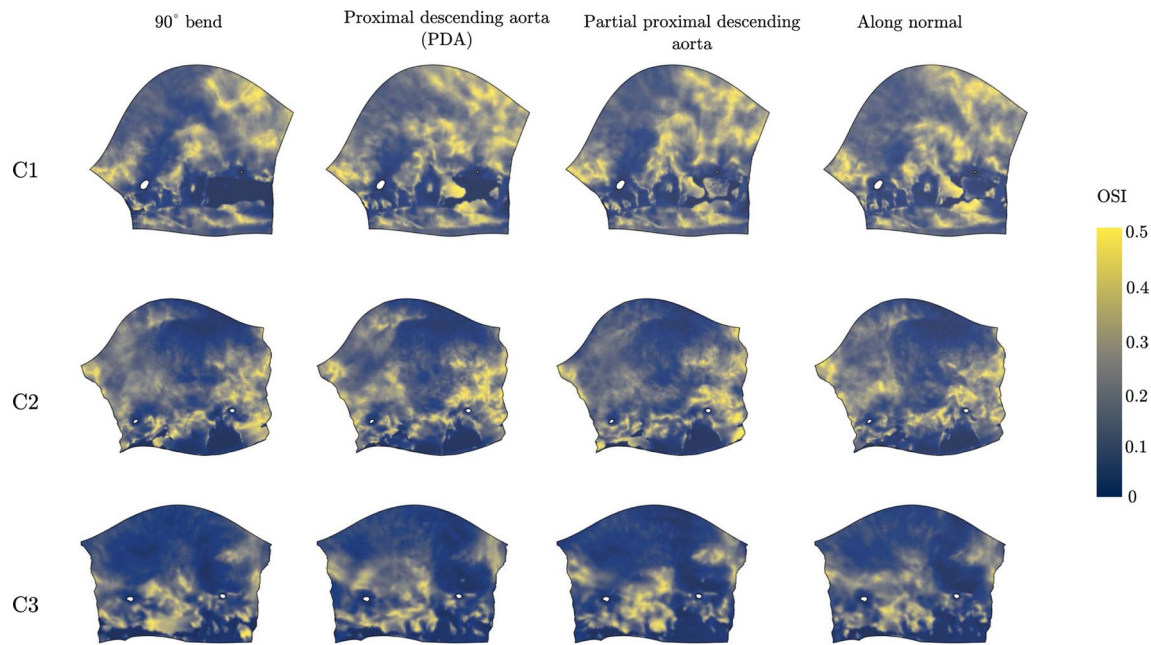


Fig. 11 TAWSS for all the configurations mapped on the parameterized 2D surface



**Fig. 12** OSI for all the configurations mapped on the parameterized 2D surface

factors that could potentially impact the region of interest. Although there are significant differences in hemodynamics distal to the ascending aorta, with sufficiently long lengths as investigated in the current work, the influence of the outflow boundaries is very minimal in and around the vicinity of the TAV. The tested modifications have not produced considerable changes for these particular anatomies with the configurations investigated both qualitatively and quantitatively. For simulating under these specific conditions, the effect of the hemodynamics within the TAVR region is minimal however, caution should be exercised when examining the region of interest further downstream.

**Supplementary Information** The online version contains supplementary material available at <https://doi.org/10.1007/s13239-024-00728-z>.

## Declarations

**Conflict of interest** Lakshmi P. Dasi is a stakeholder in DASI Simulations and has a patent pending as co-inventor of patents related to computational predictive modeling of heart valves. Other authors report no conflicts of interest. All authors have no conflict of interest relevant to this work.

## References

- Cribier, A., H. Eltchaninoff, A. Bash, N. Borenstein, C. Tron, F. Bauer, G. Derumeaux, F. Anselme, F. Laborde, and M. B. Leon. Percutaneous transcatheter implantation of an aortic valve prosthesis for calcific aortic stenosis: first human case description. *Circulation*. 106(24):3006–3008, 2002.
- Smith, C. R., M. B. Leon, M. J. Mack, D. C. Miller, J. W. Moses, L. G. Svensson, E. M. Tuzcu, J. G. Webb, G. P. Fontana, R. R. Makkar, et al. Transcatheter versus surgical aortic-valve replacement in high-risk patients. *N. Engl. J. Med.* 364(23):2187–2198, 2011.
- Leon, M. B., C. R. Smith, M. Mack, D. C. Miller, J. W. Moses, L. G. Svensson, E. M. Tuzcu, J. G. Webb, G. P. Fontana, R. R. Makkar, D. L. Brown, P. C. Block, R. A. Guyton, A. D. Pichard, J. E. Bavaria, H. C. Herrmann, P. S. Douglas, J. L. Petersen, J. J. Akin, W. N. Anderson, D. Wang, and S. Pocock. Transcatheter aortic-valve implantation for aortic stenosis in patients who cannot undergo surgery. *N. Engl. J. Med.* 363(17):1597–1607, 2010.
- Avvedimento, M., Tang, G.H.: Transcatheter aortic valve replacement (tavv): Recent updates. *Progress in Cardiovascular Diseases* (2021)
- Makkar, R. R., G. Fontana, H. Jilaihawi, T. Chakravarty, K. F. Kofoed, O. De Backer, F. M. Asch, C. E. Ruiz, N. T. Olsen, A. Trento, et al. Possible subclinical leaflet thrombosis in bioprosthetic aortic valves. *N. Engl. J. Med.* 373(21):2015–2024, 2015.
- Esmailie, F., A. Razavi, B. Yeats, S. K. Sivakumar, H. Chen, M. Samaee, I. A. Shah, A. Veneziani, P. Yadav, V. H. Thourani, et al. Biomechanics of transcatheter aortic valve replacement complications and computational predictive modeling. *Struct. Heart*.6(2):100032, 2022.
- Vahidkhan, K., M. Barakat, M. Abbasi, S. Javani, P. N. Azadani, A. Tandar, D. Dvir, and A. N. Azadani. Valve thrombosis following transcatheter aortic valve replacement: significance of blood stasis on the leaflets. *Eur. J. Cardio-Thoracic Surg.* 51(5):927–935, 2017.
- Bailoor, S., J.-H. Seo, L. P. Dasi, S. Schena, and R. Mittal. A computational study of the hemodynamics of bioprosthetic aortic valves with reduced leaflet motion. *J. Biomech.* 120:110350, 2021.
- Singh-Gryzbon, S., B. Ncho, V. Sadri, S. S. Bhat, S. S. Kollapaneni, D. Balakumar, Z. A. Wei, P. Ruile, F.-J. Neumann, P. Blanke, et al. Influence of patient-specific characteristics on transcatheter



- heart valve neo-sinus flow: an in silico study. *Ann. Biomed. Eng.* 48:2400–2411, 2020.
10. Plitman Mayo, R., H. Yaakovovich, A. Finkelstein, S. C. Shadden, and G. Marom. Numerical models for assessing the risk of leaflet thrombosis post-transcatheter aortic valve-in-valve implantation. *R. Soc. Open Sci.* 7(12):201838, 2020.
  11. Kovarovic, B. J., O. M. Rotman, P. B. Parikh, M. J. Slepian, and D. Bluestein. Mild paravalvular leak may pose an increased thrombotic risk in transcatheter aortic valve replacement (tavr) patients—insights from patient specific in vitro and in silico studies. *Bioengineering.* 10(2):188, 2023.
  12. Nicoud, F., C. Chnafa, J. Siguenza, V. Zmijanovic, and S. Mendez. Large-eddy simulation of turbulence in cardiovascular flows. *Biomed. Technol.* 8:147–167, 2018.
  13. Mittal, R., S. Simmons, and H. Udaykumar. Application of large-eddy simulation to the study of pulsatile flow in a modeled arterial stenosis. *J. Biomech. Eng.* 123(4):325–332, 2001.
  14. Chnafa, C., S. Mendez, and F. Nicoud. Image-based large-eddy simulation in a realistic left heart. *Comput. Fluids.* 94:173–187, 2014.
  15. Binder, R. K., J. Rodés-Cabau, D. A. Wood, M. Mok, J. Leipsic, R. De Larochelière, S. Toggweiler, E. Dumont, M. Freeman, A. B. Willson, et al. Transcatheter aortic valve replacement with the sapien 3: a new balloon-expandable transcatheter heart valve. *JACC.* 6(3):293–300, 2013.
  16. Pache, G., S. Schoechlin, P. Blanke, S. Dorfs, N. Jander, C. D. Arepalli, M. Gick, H.-J. Buettner, J. Leipsic, M. Langer, et al. Early hypo-attenuated leaflet thickening in balloon-expandable transcatheter aortic heart valves. *Eur. Heart J.* 37(28):2263–2271, 2016.
  17. Xu, F., S. Morganti, R. Zakerzadeh, D. Kamensky, F. Auricchio, A. Reali, T. J. Hughes, M. S. Sacks, and M.-C. Hsu. A framework for designing patient-specific bioprosthetic heart valves using immersogeometric fluid-structure interaction analysis. *Int. J. Numerical Methods Biomed. Eng.* 34(4):2938, 2018.
  18. Boufi, M., C. Guivier-Curien, A. Loundou, V. Deplano, O. Boiron, K. Chaumoitre, V. Gariboldi, and Y. Alimi. Morphological analysis of healthy aortic arch. *Eur. J. Vasc. Endovasc. Surg.* 53(5):663–670, 2017.
  19. Germano, M., U. Piomelli, P. Moin, and W. H. Cabot. A dynamic subgrid-scale eddy viscosity model. *Phys Fluids A.* 3(7):1760–1765, 1991.
  20. Lilly, D. K. A proposed modification of the Germano–Subgrid-Scale Closure method. *Phys. Fluids A.* 4(3):633–635, 1992.
  21. Pellegrini, F., Roman, J.: Scotch: A software package for static mapping by dual recursive bipartitioning of process and architecture graphs? (1996)
  22. PACE, D.: Partnership for an advanced computing environment (pace) (2017)
  23. Natarajan, T., D. E. MacDonald, M. Najafi, M. O. Khan, and D. A. Steinman. On the spectrographic representation of cardiovascular flow instabilities. *J. Biomech.* 110:109977, 2020.
  24. Lévy, B., S. Petitjean, N. Ray, and J. Maillot. Least squares conformal maps for automatic texture atlas generation. *ACM Trans. Graphics (TOG).* 21(3):362–371, 2002.
  25. Kreiser, J., M. Meuschke, G. Mistelbauer, B. Preim, and T. Ropinski. A survey of flattening-based medical visualization techniques. In: *Computer Graphics Forum*, Vol. 37, New York: Wiley, 2018, pp. 597–624.
  26. Bozzetto, M., B. Ene-Iordache, and A. Remuzzi. Transitional flow in the venous side of patient-specific arteriovenous fistulae for hemodialysis. *Ann. Biomed. Eng.* 44:2388–2401, 2016.
  27. Mancini, V., A. W. Bergersen, J. Vierendeels, P. Segers, and K. Valen-Sendstad. High-frequency fluctuations in post-stenotic patient specific carotid stenosis fluid dynamics: a computational fluid dynamics strategy study. *Cardiovasc. Eng. Technol.* 10:277–298, 2019.
  28. Valen-Sendstad, K., K.-A. Mardal, M. Mortensen, B. A. P. Reif, and H. P. Langtangen. Direct numerical simulation of transitional flow in a patient-specific intracranial aneurysm. *J. Biomech.* 44(16):2826–2832, 2011.
  29. Hunt, J.C., Wray, A.A., Moin, P.: Eddies, streams, and convergence zones in turbulent flows. Studying turbulence using numerical simulation databases, 2. In: *Proceedings of the 1988 summer program* (1988)
  30. Davies, P. F., A. Remuzzi, E. J. Gordon, C. F. Dewey Jr., and M. A. Gimbrone Jr. Turbulent fluid shear stress induces vascular endothelial cell turnover in vitro. *Proc. Natl. Acad. Sci.* 83(7):2114–2117, 1986.
  31. Boughner, D. R., and M. R. Roach. Effect of low frequency vibration on the arterial wall. *Circ. Res.* 29(2):136–144, 1971.
  32. Barakat, A. I. Blood flow and arterial endothelial dysfunction: mechanisms and implications. *Comptes Rendus Phys.* 14(6):479–496, 2013.
  33. Mamprin, M., Zelis, J.M., Tonino, P.A., Zinger, S., De With, P.H.: Identification of patients at risk of cardiac conduction diseases requiring a permanent pacemaker following tavi procedure: a deep-learning approach on ecg signals. In: *Proceedings of the 12th International Conference on Biomedical Engineering and Technology*, pp. 75–83 (2022)
  34. Biasetti, J., F. Hussain, and T. C. Gasser. Blood flow and coherent vortices in the normal and Aneurysmatic Aortas: a fluid dynamical approach to intra-luminal thrombus formation. *J. R. Soc. Interface.* 8(63):1449–1461, 2011.
  35. Ab Naim, W. N. W., P. B. Ganesan, Z. Sun, Y. M. Liew, Y. Qia, C. J. Lee, S. Jansen, S. A. Hashim, and E. Lim. Prediction of thrombus formation using vortical structures presentation in stanford type b aortic dissection: a preliminary study using cfd approach. *Appl. Math. Modell.* 40(4):3115–3127, 2016.
  36. Trusty, P. M., V. Sadri, I. D. Madukauwa-David, E. Funnell, N. Kamioka, R. Sharma, R. Makkar, V. Babaliaros, and A. P. Yoganathan. Neosinus flow stasis correlates with thrombus volume post-tavr: a patient-specific in vitro study. *JACC.* 12(13):1288–1290, 2019.
  37. Hatoum, H., J. Dollery, S. M. Lilly, J. Crestanello, and L. P. Dasi. Impact of patient-specific morphologies on sinus flow stasis in transcatheter aortic valve replacement: an in vitro study. *J. Thorac. Cardiovasc. Surg.* 157(2):540–549, 2019.
  38. Trusty, P. M., S. S. Bhat, V. Sadri, M. T. Salim, E. Funnell, N. Kamioka, R. Sharma, R. Makkar, V. Babaliaros, and A. P. Yoganathan. The role of flow stasis in transcatheter aortic valve leaflet thrombosis. *J. Thorac. Cardiovasc. Surg.* 164(3):105–117, 2022.
  39. Garcia, D., J. G. Dumesnil, L.-G. Durand, L. Kadem, and P. Pibarot. Discrepancies between catheter and doppler estimates of valve effective orifice area can be predicted from the pressure recovery phenomenon: practical implications with regard to quantification of aortic stenosis severity. *J. Am. Coll. Cardiol.* 41(3):435–442, 2003.
  40. Samaee, M., H. Hatoum, M. Biersmith, B. Yeats, S. C. Gooden, V. H. Thourani, R. T. Hahn, S. Lilly, A. Yoganathan, and L. P. Dasi. Gradient and pressure recovery of a self-expandable transcatheter aortic valve depends on ascending aorta size: in vitro study. *JTCVS Open.* 9:28–38, 2022.

**Publisher's Note** Springer Nature remains neutral with regard to jurisdictional claims in published maps and institutional affiliations.

Springer Nature or its licensor (e.g. a society or other partner) holds exclusive rights to this article under a publishing agreement with the author(s) or other rightsholder(s); author self-archiving of the accepted

manuscript version of this article is solely governed by the terms of such publishing agreement and applicable law.

## Authors and Affiliations

Thangam Natarajan<sup>1</sup> · Shelly Singh-Gryzbon<sup>1,2</sup> · Huang Chen<sup>1</sup> · Vahid Sadri<sup>1,3</sup> · Philipp Ruile<sup>4</sup> · Franz-Josef Neumann<sup>4</sup> · Ajit P. Yoganathan<sup>1</sup> · Lakshmi P. Dasi<sup>1</sup>

✉ Lakshmi P. Dasi  
lakshmi.dasi@gatech.edu

Thangam Natarajan  
thangam.natarajan@bme.gatech.edu

Shelly Singh-Gryzbon  
shelly.singh@bme.gatech.edu

Huang Chen  
huang.chen@bme.gatech.edu

Vahid Sadri  
vsadri3@gatech.edu

Philipp Ruile  
philipp.ruile@universitaets-herzzentrum.de

Franz-Josef Neumann  
franz-josef.neumann@universitaets-herzzentrum.de

Ajit P. Yoganathan  
ajit.yoganathan@bme.gatech.edu

<sup>1</sup> Department of Biomedical Engineering, Georgia Institute of Technology, 387 Technology Circle, Atlanta, GA 30313-2412, USA

<sup>2</sup> Department of Chemical Engineering, University of the West Indies, St. Augustine, Trinidad and Tobago

<sup>3</sup> Abbott Laboratories, 387 Technology Circle, Atlanta, GA 30313-2412, USA

<sup>4</sup> Department of Cardiology and Angiology, Medical Center - University of Freiburg, and Faculty of Medicine, University of Freiburg, Freiburg, Germany